Research Letter

How to Cite: *J. Inorg. Mater.*, 2026, **41(4):** 536
**DOI:** 10.15541/jim20250140

# Fabrication of Graphene-reinforced Alumina Ceramic Composites *via* Adsorption-precipitation Self-assembly Combined with Spark Plasma Sintering

CHENG Aopeng[1,2,3], WANG Yuewen[2,3,4], XU Wentao[2,5,6],
LIU Quanwei[2,3,4], ZHANG Haitao[2,5,6], ZHOU Youfu[2,5,6]

(1. College of Chemistry, Fuzhou University, Fuzhou 350108, China; 2. State Key Laboratory of Functional Crystals and Devices, Fujian Institute of Research on the Structure of Mater, Chinese Academy of Sciences, Fuzhou 350002, China; 3. Fujian College, University of Chinese Academy of Sciences, Fuzhou 350002, China; 4. College of Chemistry and Materials Science, Fujian Normal University, Fuzhou 350002, China; 5. Key Laboratory of Optoelectronic Materials Chemistry and Physics, Fujian Institute of Research on the Structure of Mater, Chinese Academy of Sciences, Fuzhou 350002, China; 6. Fujian Science & Technology Innovation Laboratory for Optoelectronic Information of China, Fuzhou 350108, China)

**Abstract:** Alumina ceramics are widely utilized as structural materials, yet their inherent brittleness and monofunctionality limit their application in high-stress scenarios. Strategic integration of two-dimensional graphene sheets, characterized by their excellent mechanical, thermal and electrical properties, into ceramic matrix can facilitate grain refinement through interface engineering, thereby achieving performance optimization. Conventional physical blending methods result in poor uniformity and integrity of 2D sheets, thereby impeding advancements in graphene-ceramic composites. Herein, a novel adsorption-precipitation self-assembly (APSA) method was proposed for the nondestructive integration of graphene oxide (GO) sheets with submicron $Al_2O_3$ particles. A homogeneous precursor is obtained by uniform deposition of $Al^{3+}$ ions adsorbed on GO surface, followed by low-temperature rapid densification *via* spark plasma sintering (SPS). For the resultant composites, the incorporated graphene is aligned parallel to the alumina grains, facilitating grain refinement and significantly enhancing the mechanical properties through synergistic effect of various toughening mechanisms, including pull-out, crack extension and bridging. In comparison to monolithic alumina ceramics, the ceramic composites exhibit a 43% enhancement in flexural strength ((428±87) MPa) and a 34% improvement in fracture toughness ((4.40±0.13) MPa·$m^{1/2}$). Furthermore, the strength and toughness values also increase by 15% respectively, compared to specimens made from the conventional ball-milling mixing process, confirming the efficacy and advancement of such a manufacturing approach.

**Key words:** graphene; alumina; ceramic composite; reinforcement; self-assembly

Alumina ($Al_2O_3$) ceramics have been extensively employed as structural materials within industrial applications, attributed to their superior properties[1]. Nevertheless, the inherent brittleness and the singular functionality of monolithic alumina limit their advanced applications. To address these drawbacks, the conventional machining constraints associated with hard ceramics can be mitigated by incorporating fracture-resistant reinforcements (*e.g.*, SiC, $ZrO_2$) to improve mechanical properties[2-4]. Additionally, doping with electrically conductive additive fillers (*e.g.*, TiC, TiN) facilitates electrical discharge machining (EDM) of complex-shaped alumina components[5-6], thereby overcoming traditional machining limitations for hard ceramics. Graphene is of great interest for its unique mechanical, electrical and thermal properties, stemming

**Received date:** 2025-04-04; **Revised date:** 2025-06-06; **Published online:** 2025-06-10
**Foundation item:** National Key Research and Development Program of China (2022YFB3708500, 2023YFB3611000); Fujian Science & Technology Innovation Laboratory for Optoelectronic Information of China (2020ZZ109); Natural Science Foundation of Fujian Province (2025H0035)
**Biography:** CHENG Aopeng (1999–), male, Master candidate. E-mail: chengaopeng@fjirsm.ac.cn
程澳芃(1999–), 男, 硕士研究生. E-mail: chengaopeng@fjirsm.ac.cn
**Corresponding author:** XU Wentao, associate professor. E-mail: wtxu@fjirsm.ac.cn
许文涛, 副研究员. E-mail: wtxu@fjirsm.ac.cn

from the 2D honeycomb lattice structure. The available graphene-derived materials encompass tailored architectures with controlled layer numbers and lateral dimensions, such as few-layer graphene (FLG), multi-layer graphene (MLG), and graphene nanoplatelets (GNPs), *etc*. Furthermore, graphene with different oxygen contents, including graphene oxide (GO) and reduced graphene oxide (rGO), has been developed, demonstrating favorable surface modifiability and aqueous dispersibility due to the abundance of terminal groups[7-8]. Such structural versatility positions graphene-based materials as promising candidates for the toughening alumina ceramics[9-11].

However, the fabrication of graphene-ceramic composites with high quality is impeded by several critical challenges. (1) Graphene tends to agglomerate, resulting in uneven distribution within the ceramic matrix[12]. (2) Maintaining the structural integrity of graphene during the processing is difficult[13]. (3) The insufficient bonding between graphene and matrix undermines load transfer efficiency, leading to the diminished strength[14]. Researchers have made some attempts to prepare graphene-$Al_2O_3$ ceramic composites. For instance, Chen *et al*.[15] developed GNPs/$Al_2O_3$ composites through a combination of ball milling and hot pressing (HP), which notably enhanced fracture toughness of the resultant ceramic composites. Nieto *et al*.[16] successfully incorporated a high volume fraction (5%–15%) of GNPs into an $Al_2O_3$ matrix using ultrasonic and ball milling techniques, subsequently fabricating GNPs-$Al_2O_3$ ceramic composites *via* spark plasma sintering (SPS). Although the introduction of GNPs resulted in a decrease in hardness, the toughness of the composite ceramic was increased. Dhar *et al*.[17] prepared rGO-$Al_2O_3$ composite powders using ball milling, followed by sintering under argon environment. It was found that the hardness and Young's modulus were enhanced. However, a further increase in rGO led to agglomeration of graphene flakes, consequently reducing the mechanical properties. In most of the existing studies, the dispersion of graphene was achieved through prolonged ball milling, which failed to ensure good homogeneity and structural integrity. Previously, a self-assembly technology for nanoparticles and two-dimensional materials has been developed, which optimizes the incorporating process and improves the performance of the ceramic composites to a certain extent[18-19].

In this work, an adsorption-precipitation self-assembly (APSA) approach was proposed to achieve pre-mixing and synchronous settling of alumina ceramic particles with graphene sheets in solution, thereby yielding uniform and undamaged composite powders. Based on the electrostatic interaction, $Al^{3+}$ ions were adsorbed onto the surface of graphene oxide, forming a colloidal dispersion. Subsequently, the precipitation of metal ions was induced to encapsulate the graphene sheets, forming a homogeneous precursor. Consequently, thermal reduction and SPS were carried out to fabricate a series of rGO-$Al_2O_3$ ceramic composites with improved mechanical and functional properties. This study thoroughly investigated the microstructure evolution of the grains and graphene sheets, elucidating the mechanism of strengthening and toughening, as well as the improvement in enhanced electrical and thermal conductivity.

# 1 Experimental

## 1.1 Preparation of rGO-$Al_2O_3$ powders

As shown in Fig. 1, the hybrid precursor was initially prepared by a developed APSA method. In this process, GO was firstly prepared *via* a modified Hummers method. Subsequently, a certain amount of GO was dispersed in deionized water and sonicated for 1 h by the ultrasound probe (Scientz-1500F, Scientz) to obtain the transparent dispersion of GO. Following this, various volumes of $Al(NO_3)_3$ solution with a certain concentration were dropped into the GO dispersion and thoroughly stirred, targeting GO mass fractions in $Al_2O_3$ of 0.5%, 1.0%, 2.0%, 3.0%, 4.0% and 5.0%, respectively. The resultant mixed solution was then gradually added to the ammonium bicarbonate solution and stirred for 2 h followed by filtration and washing with deionized water. Then, the precipitates were then freeze-dried to obtain the precursors. Further calcination of these precursors was performed at 600 ℃ for 1 h under nitrogen atmosphere, effectively removing the adsorbed moisture and carbonate while converting GO into rrGO. The obtained composite powders were designated as 0.5rGO-$Al_2O_3$, 1rGO-$Al_2O_3$, 2rGO-$Al_2O_3$, 3rGO-$Al_2O_3$, 4rGO-$Al_2O_3$, and 5rGO-$Al_2O_3$ powders, respectively. As a reference, pure $Al_2O_3$ powders without GO addition were prepared following the same process.

## 1.2 Sintering of rGO-$Al_2O_3$ ceramic composites

The dense ceramics were prepared by SPS equipment (Dr. Sinter 211, Fuji). The specific preparation conditions were as follows: a graphite mold with an inner diameter of 20 mm was used at a heating rate of 100 ℃/min and a uniaxial pressure of 50 MPa. The mold was maintained at the target temperature for 5 min. In order to determine the optimal parameters, samples with 5.0% rGO were sintered at different temperatures (1200–1400 ℃). Concurrently, samples with different rGO contents were sintered at 1350 ℃ for comparative analyses, labeled as 0.5rGO-$Al_2O_3$, 1rGO-$Al_2O_3$, 2rGO-$Al_2O_3$, 3rGO-$Al_2O_3$, 4rGO-$Al_2O_3$, and 5rGO-$Al_2O_3$ ceramic composites, respectively.

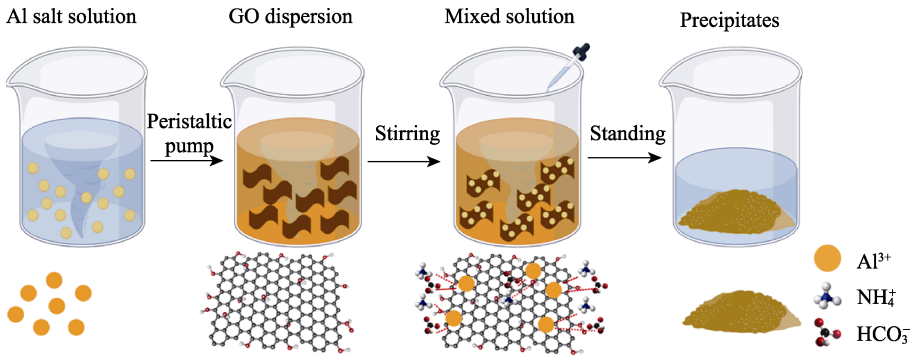


Fig. 1 Schematic illustration of preparing process for hybrid precursors by APSA method

### 1.3 Characterization

The Zeta potential of GO dispersion was tested by a BI-200SM research-grade light scattering system (Brookhaven Instruments) across a pH range of 3–11 (adjusted with $HNO_3$ and NaOH solutions). The phase composition of hybrid powders and ceramics was identified by X-ray diffractometer (XRD, Miniflex 600, Rigaku) using Cu K$\alpha$ radiation. Raman spectra of the samples were analyzed using an *in-situ* confocal Raman spectrometer (Lab RAM HR Evolution) with a light source wavelength of 532 nm and an exposure time of 10 s. Morphology and microstructure of the powders and composites were characterized using scanning electron microscope (SEM, SU-8010, Hitachi), equipped with an energy dispersive spectroscopy (EDS) apparatus. The thermogravimetric analysis (TGA, STA 449F3, Netzsch) of the samples was performed in nitrogen until reaching 900 ℃ at a heating rate of 10 ℃/min.

The density of bulk was measured by the Archimedes method by a density balance (GH-300C, Xiamen Group Lung Instrument Co., Ltd.). Vickers hardness was assessed on the polished surface using a visual Vickers hardness tester (MHVS-10V, AOLONG) under a loading force of 9.8 N for 10 s. For each group of samples, five measurement points were selected and the average value was taken as the final result. The flexural strength of strip specimens measuring 18 mm×2 mm×1.5 mm was evaluated using a universal testing machine (UTM304X, SUNS) through the three-point bending method, with a span of 15 mm. The loading rate was maintained at 0.5 mm/min. Each specimen underwent five tests, and the mean value was calculated for analysis. Fracture toughness was assessed using indentation method, with corresponding values calculated according to Evans' formula (Eq. (1)):

$$K_{IC}=0.16H_v a^2 c^{-1.5} \quad (1)$$

where $K_{IC}$ represents the fracture toughness, $H_v$ denotes the microhardness under the same pressure, and $a$ and $c$ are the half-length of the diagonal indentation and cracking, respectively.

Electrical conductivity measurements by the four-probe method (RTS-9 tester, 4 Probes Tech) were performed on different surfaces of strip specimens (the surface parallel and perpendicular to the sintering pressure) across at least five different positions, denoted as $\sigma_\perp$ and $\sigma_\parallel$. The thermal diffusivity ($\alpha$) and heat capacity ($C_P$) of the samples were measured by laser flash method (LFA467, Netzsch). The dimension of the sample with polished surfaces was 10 mm×10 mm×1.5 mm. The thermal conductivity ($\lambda$) was calculated by Eq. (2):

$$\lambda=\alpha\cdot C_P\cdot\rho \quad (2)$$

where $\alpha$ is the determined thermal diffusivity, $C_P$ is the specific heat capacity, and $\rho$ is the density.

## 2 Results and discussion

### 2.1 Characterization of rGO-$Al_2O_3$ powders

The oxygen-containing functional groups on the surface of GO sheets confer significant hydrophilicity, thus providing a natural advantage in the formulation of highly dispersible aqueous solutions. The stability of the resulting GO colloids is critical for the preparation of homogeneous precursors, which is closely related to the surface properties of the nanosheets. Characterization results of GO are shown in Fig. S1. Zeta potential of the GO dispersion is observed to remain around –20 mV across a wide pH range from 3 to 11 (Fig. 2(a)). This negatively charged surface facilitates the stable dispersion of GO nanosheets and establishes favorable conditions for fabrication of hybrid precursors by APSA method. With the mixing of $Al^{3+}$ ions, they are adsorbed and eventually localized on the GO sheet surface due to electrostatic interactions[20]. The Zeta potential of the aqueous GO dispersion changes from negative to positive (from –20 mV to +10 mV) with $Al^{3+}$ ions addition, indicating charge neutralization resulting from coordination between $Al^{3+}$ and oxygen-containing functional groups on the GO. It is also found that the absolute value of the Zeta potential gradually decreases, leading to agglomeration and sedimentation of GO sheets.

This phenomenon can be attributed to the adsorption of $Al^{3+}$ on the GO surface, which disrupts the electrostatic repulsion between the GO sheets and reduces colloidal stability of dispersion. Subsequent addition of bicarbonate as a precipitant for $Al^{3+}$ ions induces rapid formation of deposits on the GO surface, which allows for the self-assembly of all components to homogeneous hybrids and simultaneous settling. The precipitated particles anchored on GO surface effectively prevent 2D sheets from restacking due to π-electron interaction. In addition, this *in-situ* compounding method, which does not require mechanical blending such as ball milling, avoids structural damage to nanosheets.

Pre-calcination temperature of 600 ℃ was determined by TGA analysis (Fig. S2). XRD patterns of the precursors before and after calcination exhibit no significant diffraction peaks (Fig. 2(b)), suggesting that the synthesized composite powders are amorphous, while GO is below the detection limit due to its low content. SEM image shown in Figs. 2(c, d) reveals the morphology of the precursor and calcinated powders. These particles exhibit a generally spherical shape, with sizes less than 100 nm, uniformly adhering to graphene sheets, and forming small aggregates separated by the curved and folded 2D nanosheets.

## 2.2 Characterization of rGO-$Al_2O_3$ ceramic composites

As illustrated in Fig. S3, sintering temperature of the ceramic composites is determined to be 1350 ℃ *via* densification studies. Fig. S4 shows the composition of rGO-$Al_2O_3$ ceramics, revealing pure $\alpha$-$Al_2O_3$ phase for all specimens sintered at different temperatures and with different rGO contents (1350 ℃). To investigate the structure evolution of graphene in composites, Raman spectra were performed (Fig. S5).

## 2.3 Microstructure of rGO-$Al_2O_3$ ceramic composites

Fig. 3 presents the SEM images of the fractured surfaces of the ceramic composites, revealing a homogenous dense structure and dominant intergranular fracture mode as a result of rGO addition. The average grain size of $Al_2O_3$ decreases from 2.5 μm to 1.3 μm with increasing rGO content, as determined by counting all grains in the images. Few-layered flakes, with thickness of approximately a few tens of nanometers, are uniformly distributed at the grain boundaries with slight wavy edges. A small amount of porosity is observed at the interface between the sheets and the grains. Notably, two-dimensional materials typically align along the sintering pressure direction due to their planar geometry. Consequently, the rGO-$Al_2O_3$ ceramic here exhibits this characteristic, with the nanosheets primarily oriented in parallel. According to EDS mappings (Fig. S6), the distribution of C element is observable, yet accurate quantification remains challenging.

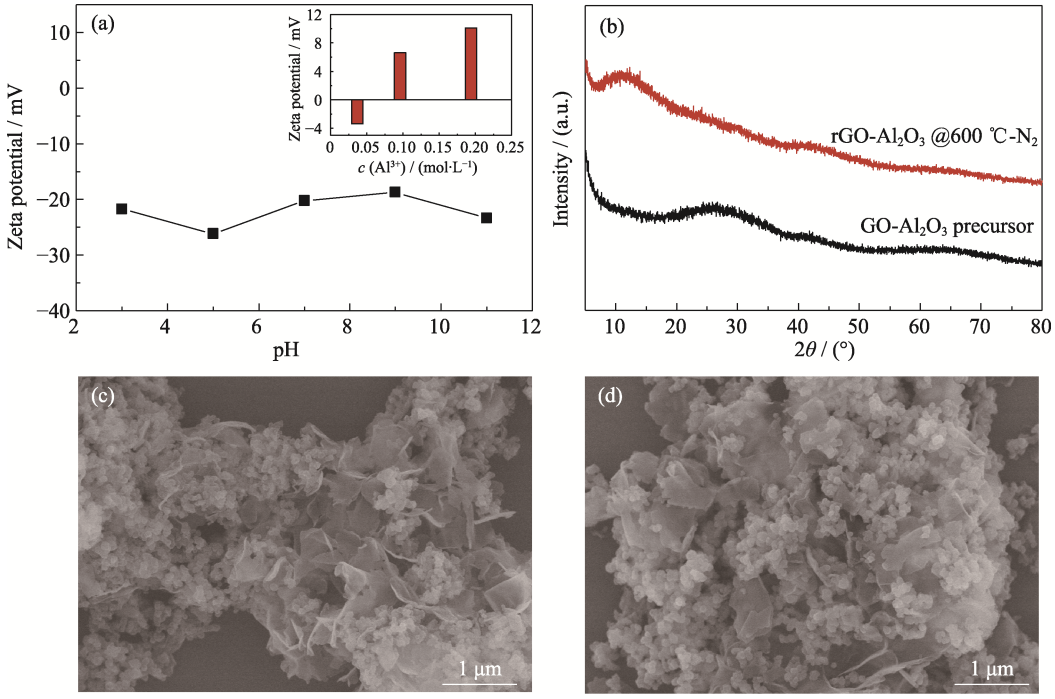


Fig. 2 (a) Zeta potential of GO dispersion as a function of pH with inset showing the Zeta potentials for different $Al^{3+}$ ions added to the GO solution; (b) XRD patterns of the precursors before and after calcination; (c, d) SEM images of 5rGO-$Al_2O_3$ precursor (c) before and (d) after calcinations

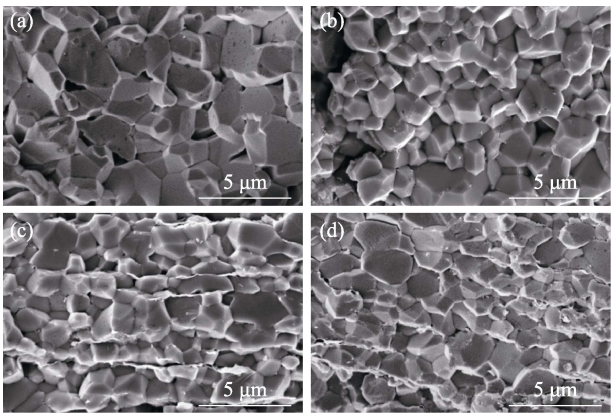


Fig. 3 Fracture surface morphologies of the SPSed ceramics
(a) Monolithic $Al_2O_3$; (b) 1rGO-$Al_2O_3$; (c) 3rGO-$Al_2O_3$; (d) 5rGO-$Al_2O_3$

## 2.4 Mechanical properties

The mechanical properties of the ceramic as a function of rGO content are shown in Fig. 4. As the rGO content increases, the density of the ceramic composites continues to decrease, which can be attributed to the inherent low density of rGO and the introduction of residual porosity[21](Fig. 4(a)). Regarding the Vickers hardness of the ceramic composites, an initial slight increase in hardness is observed with increasing rGO content, followed by a gradual decrease (Fig. 4(b)). The hardness peaks at (19.93±0.20) GPa when the mass fraction of rGO reaches 0.5%. The enhancement can be attributed to the grain size refining by incorporation of nanosheets. The reduced hardness can be attributed to the intrinsic soft properties of rGO (hardness of 1 GPa), as well as its plastic deformation[22].

Upon doping a small quantity of rGO, the flexural strength of the composite attains a maximum value of (428±87) MPa for the 1rGO-$Al_2O_3$ composite, representing a 43% enhancement compared to the monolithic ceramic (Fig. 4(c)). In accordance with the Hall-Petch relationship, the addition of rGO results in grain refinement, thereby enhancing the flexural strength of ceramic composites. Furthermore, the embedded rGO sheets hinder crack propagation by necessitating additional energy for their pullout or bending, thereby enhancing the composite's load-bearing capacity and further improving its flexural strength. Conversely, when the rGO content exceeds 1.0%, a conspicuous decline in flexural strength is observed, which can be primarily attributed to three factors: weak bonding strength between the graphene sheets and the ceramic matrix, severe agglomeration of graphene at elevated concentrations[23], and increased wrapped porosity at the boundaries.

Fig. 4(d) shows the indentation fracture toughness of rGO-$Al_2O_3$ composites, calculated using Evans' empirical formula. With an increase in graphene content, the fracture toughness initially rises to (4.40±0.13) MPa·$m^{1/2}$ for the 1rGO-$Al_2O_3$, which corresponds to a 34% enhancement over the monolithic ceramic. Grain refinement also dissipates fracture energy through the hindrance of crack propagation by rGO, causing crack propagation to preferentially occur along rGO interfaces and consume additional energy, thus improving the fracture toughness of the material[24]. Furthermore, residual stresses arising from the thermal expansion coefficient (CTE) mismatch between rGO (negative CTE) and $Al_2O_3$ ($5.8\times10^{-6}$ $K^{-1}$) must be considered. These stresses induce localized microcracks that create plastic zones at the tips of main crack, activating crack deflection mechanisms that synergistically improve fracture toughness[25]. Elevated rGO doping level induces micropore proliferation, thereby degrading toughness due to the accumulation of structural defects.

The shape of the curves given in Fig. 4 suggests a relation between strength and fracture toughness, as both properties increase with the addition of rGO before exhibiting a continuous decrease. The relationship between fracture toughness and fracture strength is given by the following equation[26]:

$$\sigma_f = \sqrt{\pi}/2 \cdot K_{IC} \cdot C^{1/2} \quad (3)$$

where $K_{IC}$ is the fracture toughness, $\sigma_f$ is the flexural strength, and $C$ is the critical penny-shaped crack radius. Thus, the factors controlling strength also control the fracture toughness of the ceramic composites, including porosity level and morphology of the $Al_2O_3$ grains and rGO sheets.

The growth mechanisms in the monolithic $Al_2O_3$ samples are arrested by the presence of rGO. Dense samples possessing high fracture toughness, small grain size and small inherent flaw size are expected to achieve optimal strength[27].

For comparative purposes, composite powders were also synthesized by ball-milling aluminum-containing precursors (obtained *via* the precipitation method) with graphene oxide, and related ceramic composites (0.5rGO-$Al_2O_3$-bm and 1rGO-$Al_2O_3$-bm) were prepared under the same sintering conditions. The mechanical properties of these samples were inferior to those of counterparts obtained by APSA method, thereby confirming the advantage of this method in fabricating graphene-reinforced ceramics. The properties of the samples prepared in this work are summarized in Table 1 with the values reported in the literatures[11, 28-30], demonstrating their good performance.

The primary toughening mechanisms of rGO in $Al_2O_3$ ceramic include plate pullout, crack deflection, and

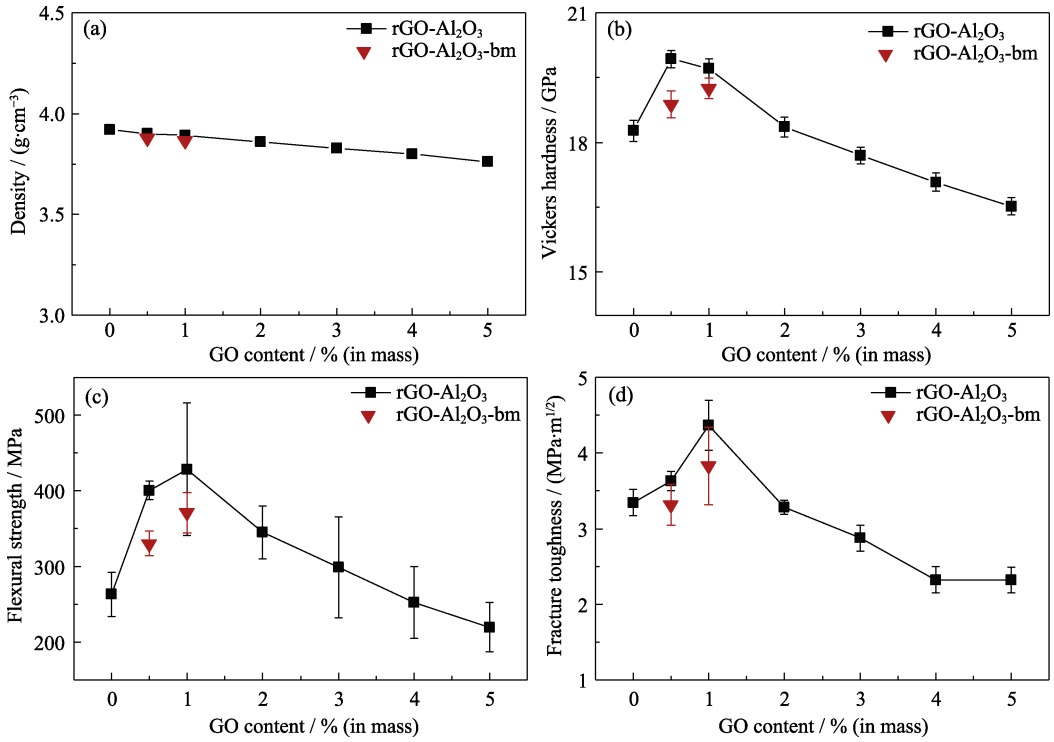


Fig. 4 Mechanical properties of rGO-$Al_2O_3$ ceramic composites
(a) Density; (b) Vickers hardness; (c) Flexural strength; (d) Fracture toughness

bridging, as depicted in Fig. 5. Graphene incorporation disrupts the stress field at the crack tip, thereby promoting crack propagation along the interface of 2D sheet[31]. This phenomenon leads to a serpentine-like crack pattern, which extends the propagation path and enhances energy dissipation. Simultaneously, graphene bridging can inhibit crack tip opening, thus preventing fracture progression[21]. As external loading increases, graphene progressively delaminates and is extracted. Moreover, the addition of GO leads to C doping to some extent, which can enhance the grain boundary strength of ceramics[32]. Thus, in rGO-$Al_2O_3$ ceramics, multiple toughening mechanisms act synergistically.

## 2.5 Electrical and heat conductivity

GO exhibits electrical insulating behavior owing to the disrupted $sp^2$ hybridized carbon network[33]. Subsequent thermal treatment and sintering (SPS) facilitate the decomposition and removal of oxygen-containing functional groups in GO, yielding rGO with a partial restoration of electrical conductivity. Fig. 6(a) illustrates the electrical conductivity evolution in ceramic composites with varying rGO contents. Specimens containing 0.5% and 1.0% rGO exhibit immeasurably high electrical resistance (>$10^6$ Ω·m), while 2rGO-$Al_2O_3$ composite achieves a conductivity of 6.7 S·$m^{-1}$. Notably, mass loss during thermal processing results in actual rGO content being lower than nominal values, indicating a reduced percolation threshold in comparison to theoretical predictions. Conductivity increased exponentially to

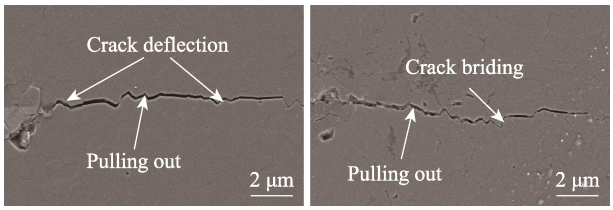


Fig. 5 Crack propagation and toughening mechanisms in rGO-$Al_2O_3$ ceramic composites

**Table 1 Characteristics and properties of the graphene-$Al_2O_3$ ceramic composites[11, 28-30]**

| Material | Filler loading/ % (in mass) | Sintering method | Vickers hardness/ GPa | Fracture toughness/ (MPa·$m^{1/2}$) | Flexural strength/ MPa | Reference |
|---|---|---|---|---|---|---|
| rGO-$Al_2O_3$ | 1.0 | SPS | 19.71 | 4.4 | 428 | This work |
| rGO-$Al_2O_3$ | 3.0 | HP | 9.9 | — | 313.75 | [11] |
| GO-$Al_2O_3$ | 0.5 | SPS | 18.3 | 5.4 | — | [28] |
| FLG-$Al_2O_3$ | 1.0 | SPS | 20.1 | 3.3 | 310 | [29] |
| GNP-$Al_2O_3$ | 0.5 | HP | 17 | 5.5 | 390 | [30] |

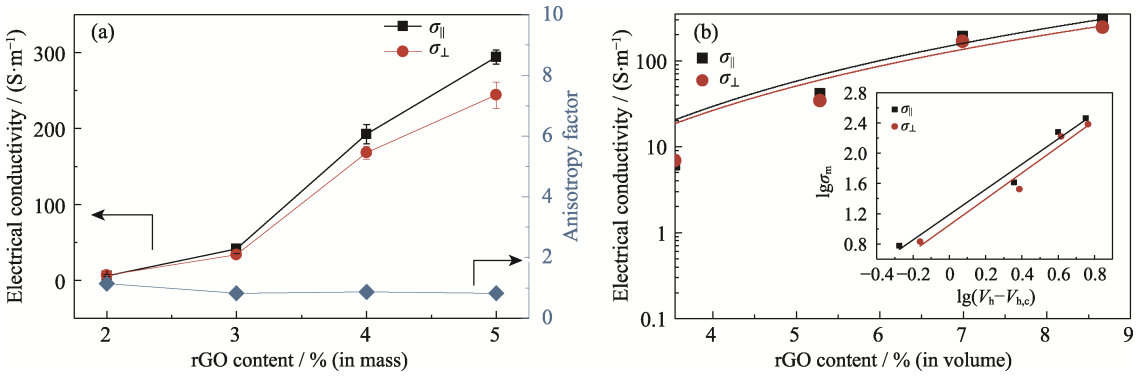


Fig. 6 (a) Electrical conductivity of rGO-$Al_2O_3$ composites as a function of filler fraction in two directions; (b) Fitting curves of electrical conductivity with inset showing the logarithmic plots of electrical conductivities against ($V_h$–$V_{h,c}$)

294.1 S·m$^{-1}$ at 5.0% rGO loading, which can be attributed to the formation of interconnected three-dimensional conductive networks through graphene sheet penetration[34]. Remarkably, the composites demonstrate isotropic electrical properties, with comparable surface conductivities in directions parallel ($\sigma_{\parallel}$) and perpendicular ($\sigma_{\perp}$) to the sintering pressure axis. This directional uniformity suggests an effective random orientation of rGO flakes within the ceramic matrix at higher doping levels.

The electrical conductivity evolution follows the percolation theory as expressed by Eq. (4)[35]:

$$\sigma_m=\sigma_h(V_h-V_{h,c})^t \quad (4)$$

where $\sigma_m$ and $\sigma_h$ represent the composite and conductive filler conductivities, respectively, $V_h$ is the filler volume fraction, $V_{h,c}$ is the percolation threshold, and $t$ is the universal critical exponent.

As shown in Fig. 6(b), experimental data fitting (with a density of $Al_2O_3$ at 3.97 g·cm$^{-3}$, while that of graphene at 2.20 g·cm$^{-3}$) yields percolation thresholds of 3.02% ($\sigma_{\perp}$, in volume) and 2.78% ($\sigma_{\parallel}$, in volume), with corresponding $t$ values of 1.68 and 1.25, respectively. These exponents deviate from classical 3D ($t$=2.0) or 2D ($t$=1.3) conduction models[36], indicating hybrid conductive networks. The higher number of "dead arms" in this structure, compared to the classical random morphology, may be responsible[37-38]. This phenomenon is similar to that observed in other graphene-ceramic composites[18].

Fig. S7 illustrates the thermal conductivity ($\kappa$) of the ceramic composites within the temperature range of 25–300 ℃. The thermal conductivity of $Al_2O_3$ is measured at 30.92 W·m$^{-1}$·K$^{-1}$, with addition of 2.0% rGO slightly enhancing the thermal conductivity of the composite (2rGO-$Al_2O_3$) to 31.32 W·m$^{-1}$·K$^{-1}$. This improvement is attributed to the intrinsic high thermal conductivity of rGO and the establishment of a more efficient heat transfer network within the matrix. However, as the rGO content further increases, the thermal conductivity of the composites significantly decreases (*e.g.*, 5rGO-$Al_2O_3$, 18.22 W·m$^{-1}$·K$^{-1}$). This reduction may be a result of the increased porosity in the matrix, which produces more phonon scattering. Additionally, the interfacial thermal resistance between rGO and grain boundary, alongside the curling and aggregation of rGO sheets, further degrades the heat transfer efficiency.

## 3 Conclusions

In this work, a novel APSA strategy was proposed to fabricate graphene-incorporated $Al_2O_3$ composites. The method facilitates rapid and non-destructive mixing of GO sheets with $Al_2O_3$ particles, which can subsequently be densified at 1350 ℃ by SPS. The resultant homogeneous distribution and complete 2D morphology of fillers ensure a refined microstructure, endowing rGO-$Al_2O_3$ ceramic composites with superior mechanical performance and electrical conductivity compared to samples prepared by ball milling mixing. The 1rGO-$Al_2O_3$ composite demonstrates exceptional mechanical properties, wherein the Vickers hardness of the material is measured at 19.71 GPa, and its flexural strength is determined to be 428 MPa. The fracture toughness is enhanced to 4.4 MPa·m$^{1/2}$ through synergistic toughening mechanisms. Simultaneously, the percolating rGO network enables tunable electrical conductivity (6.7–294.1 S·m$^{-1}$) with a low percolation threshold (2.78%, in volume) based on the mixed conductive mode. Moreover, a high thermal conductivity (31.32 W·m$^{-1}$·K$^{-1}$) superior to monolithic $Al_2O_3$ can be achieved when 2% rGO is added. This general APSA method can be extended to other ceramic composites conveniently. Encouraged by

the high overall performance, further researches are underway to explore the design, and fabrication of such rGO doped ceramics.

## Supporting Materials

Supporting materials related to this article can be found at https://doi.org/10.15541/jim20250140.

### References:


[1] MUDRA E, HRUBOVCAKOVA M, SHEPA I, *et al*. Processing and characterization of fiber-reinforced and layered alumina-graphene composites. *Journal of the European Ceramic Society*, 2020, **40(14):** 4808.

[2] GEVORKYAN E, RUCKI M, PANCHENKO S, *et al*. Effect of SiC addition to $Al_2O_3$ ceramics used in cutting tools. *Materials*, 2020, **13(22):** 5195.

[3] WANG H Z, GAO L, GUO J K. Silicon carbide particle size effects in $Al_2O_3$-SiC nanocomposites. *Journal of Inorganic Materials*, 1999, **14(4):** 679.

[4] OJAIMI C L, FERREIRA J A, DOS SANTOS F A, *et al*. Mechanical characterization and hydrothermal degradation of $Al_2O_3$-15 vol% $ZrO_2$ nanocomposites consolidated by two-step sintering. *Ceramics International*, 2018, **44(14):** 16128.

[5] XU C H, HUANG C Z, LI Z Q, *et al*. Toughening mechanisms of $Al_2O_3$/TiC ceramic composite with carbon additive. *Journal of Inorganic Materials*, 2001, **16(2):** 256.

[6] BAGHEL R, MALI H S, BISWAS S K. Micro hole fabrication in TiN-$Al_2O_3$ ceramic composite by SiC powder assisted micro-EDM. *Engineering Research Express*, 2020, **2(1):** 15028.

[7] ZHU Y, MURALI S, CAI W, *et al*. Graphene and graphene oxide: synthesis, properties, and applications. *Advanced Materials*, 2010, **22(35):** 3906.

[8] FARJADIAN F, ABBASPOUR S, SADATLU M A A, *et al*. Recent developments in graphene and graphene oxide: properties, synthesis, and modifications: a review. *ChemistrySelect*, 2020, **5(33):** 10200.

[9] LI W, SIM H J, LU H, *et al*. Effect of reduced graphene oxide on the mechanical properties of rGO/$Al_2O_3$ composites. *Ceramics International*, 2022, **48(16):** 24021.

[10] SHIN J H, CHOI J, KIM M, *et al*. Comparative study on carbon nanotube- and reduced graphene oxide-reinforced alumina ceramic composites. *Ceramics International*, 2018, **44(7):** 8350.

[11] ZHOU L, QIU J, WANG X, *et al*. Mechanical and dielectric properties of reduced graphene oxide nanosheets/alumina composite ceramics. *Ceramics International*, 2020, **46(12):** 19731.

[12] MARKANDAN K, CHIN J K, TAN M T T. Recent progress in graphene based ceramic composites: a review. *Journal of Materials Research*, 2016, **32(1):** 84.

[13] BARTOLUCCI S F, PARAS J, RAFIEE M A, *et al*. Graphene–aluminum nanocomposites. *Materials Science and Engineering: A*, 2011, **528(27):** 7933.

[14] SUN C, HUANG Y, SHEN Q, *et al*. Embedding two-dimensional graphene array in ceramic matrix. *Science Advances*, 2020, **6(39):** eabb1338.

[15] CHEN Y F, BI J Q, YIN C L, *et al*. Microstructure and fracture toughness of graphene nanosheets/alumina composites. *Ceramics International*, 2014, **40(9):** 13883.

[16] NIETO A, HUANG L, HAN Y H, *et al*. Sintering behavior of spark plasma sintered alumina with graphene nanoplatelet reinforcement. *Ceramics International*, 2015, **41(4):** 5926.

[17] DHAR S, DASH T, SAHU A K, *et al*. Study on the microstructure and microhardness behavior of reduced graphene oxide reinforced alumina nanocomposites. *Journal of Materials Engineering and Performance*, 2024, **33(11):** 5446.

[18] WU J, XU W, DONG T, *et al*. Self-assembly of graphene reinforced $ZrO_2$ composites with deformation-sensing performance. *Ceramics International*, 2022, **48(21):** 32131.

[19] DONG T, XU W, JIN M, *et al*. A self-assemble strategy toward conductive 2D MXene reinforced $ZrO_2$ composites with sensing performance. *Journal of the European Ceramic Society*, 2022, **42(3):** 1102.

[20] ZHAO G K, ZHU H W. Cation-π interactions in graphene-containing systems for water treatment and beyond. *Advanced Materials*, 2020, **32(22):** 1905756.

[21] LIU J, YAN H X, JIANG K. Mechanical properties of graphene platelet-reinforced alumina ceramic composites. *Ceramics International*, 2013, **39(6):** 6215.

[22] MAZAHERI M, MARI D, SCHALLER R, *et al*. Processing of yttria stabilized zirconia reinforced with multi-walled carbon nanotubes with attractive mechanical properties. *Journal of the European Ceramic Society*, 2011, **31(14):** 2691.

[23] BOBYLEV S V, SHEINERMAN A G. Effect of crack bridging on the toughening of ceramic/graphene composites. *Reviews on Advanced Materials Science*, 2018, **57(1):** 54.

[24] WOZNIAK J, PETRUS M, CYGAN T, *et al*. Silicon carbide matrix composites reinforced with two-dimensional titanium carbide – manufacturing and properties. *Ceramics International*, 2019, **45(6):** 6624.

[25] LU S, LI X Q, ZHOU Y F, *et al*. Synthesis and mechanical properties of $TiB_2$/$Ti_2AlN$ composites fabricated by hot pressing sintering. *Journal of the Ceramic Society of Japan*, 2018, **126(11):** 900.

[26] AHMOYE D, BUCEVAC D, KRSTIC V D. Mechanical properties of reaction sintered SiC-TiC composite. *Ceramics International*, 2018, **44(12):** 14401.

[27] WANG G, KRSTIC V D. Roles of porosity, residual stresses and grain size in the fracture of brittle solids. *Philosophical Magazine A*, 1998, **78(5):** 1125.

[28] WOZNIAK J, JASTRZĘBSKA A, CYGAN T, *et al*. Surface modification of graphene oxide nanoplatelets and its influence on mechanical properties of alumina matrix composites. *Journal of the European Ceramic Society*, 2017, **37(4):** 1587.

[29] HRUBOVCAKOVA M, MUDRA E, BURES R, *et al*. Microstructure, fracture behaviour and mechanical properties of conductive alumina based composites manufactured by SPS from graphenated $Al_2O_3$ powders. *Journal of the European Ceramic Society*, 2020, **40(14):** 4818.

[30] YAZDANI B, XU F, AHMAD I, *et al*. Tribological performance of graphene/carbon nanotube hybrid reinforced $Al_2O_3$ composites. *Scientific Reports*, 2015, **5:** 11579.

[31] WALKER L S, MAROTTO V R, RAFIEE M A, *et al*. Toughening in graphene ceramic composites. *ACS Nano*, 2011, **5(4):** 3182.

[32] YAHYA N A, TODD R I. Influence of C doping on the fracture mode and abrasive wear of $Al_2O_3$. *Journal of the European Ceramic Society*, 2012, **32(16):** 4003.
[33] MCALLISTER M J, LI J L, ADAMSON D H, *et al*. Single sheet functionalized graphene by oxidation and thermal expansion of graphite. *Chemistry of Materials*, 2007, **19(18):** 4396.
[34] FAN Y, JIANG W, KAWASAKI A. Highly conductive few-layer graphene/$Al_2O_3$ nanocomposites with tunable charge carrier type. *Advanced Functional Materials*, 2012, **22(18):** 3882.
[35] CINAR A, BASKUT S, SEYHAN A T, *et al*. Tailoring the properties of spark plasma sintered SiAlON containing graphene nanoplatelets by using different exfoliation and size reduction techniques: anisotropic mechanical and thermal properties. *Journal of the European Ceramic Society*, 2018, **38(4):** 1299.
[36] FAN Y C, WANG L J, LI J L, *et al*. Preparation and electrical properties of graphene nanosheet/$Al_2O_3$ composites. *Carbon*, 2010, **48(6):** 1743.
[37] KILBRIDE B E, COLEMAN J N, FRAYSSE J, *et al*. Experimental observation of scaling laws for alternating current and direct current conductivity in polymer-carbon nanotube composite thin films. *Journal of Applied Physics*, 2002, **92(7):** 4024.
[38] AHMAD K, PAN W, SHI S L. Electrical conductivity and dielectric properties of multiwalled carbon nanotube and alumina composites. *Applied Physics Letters*, 2006, **89(13):** 133122.

# 吸附-沉淀自组装结合放电等离子烧结法制备石墨烯增强氧化铝复合陶瓷

程澳芃[1,2,3], 王跃文[2,3,4], 许文涛[2,5,6], 刘全伟[2,3,4], 张海涛[2,5,6], 周有福[2,5,6]

(1. 福州大学 化学学院, 福州 350108; 2. 中国科学院 福建物质结构研究所, 功能晶体与器件全国重点实验室, 福州 350002; 3. 中国科学院大学 福建学院, 福州 350002; 4. 福建师范大学 化学与材料科学学院, 福州 350002; 5. 中国科学院 福建物质结构研究所, 光电材料化学与物理重点实验室, 福州 350002; 6. 福建光电信息科技创新实验室, 福州 350108)

**摘 要:** 氧化铝陶瓷是广泛应用的结构材料, 但固有脆性和单一功能限制了其在高性能要求环境中的应用。二维石墨烯具有优异的机械、热和电特性, 将其组装入陶瓷基体, 可通过界面工程促进晶粒细化, 实现性能优化。传统的物理混合方法导致石墨烯片的均匀性和完整性较差, 阻碍了复合材料的发展。针对上述问题, 本工作提出了一种新型的吸附沉淀自组装(APSA)方法, 能够实现氧化石墨烯(GO)薄片与亚微米 $Al_2O_3$ 颗粒无损复合。通过在 GO 表面吸附 $Al^{3+}$离子实现均匀沉积, 可获得均匀前驱体, 进一步结合放电等离子烧结(SPS)可实现低温快速致密化。在制备的复合陶瓷中, 石墨烯沿着氧化铝晶粒平行排列, 促进了晶粒细化, 并通过拉出、裂纹扩展和桥接等多种增韧机制的协同作用显著提高了材料的机械性能。与单一氧化铝陶瓷相比, 复合陶瓷的抗弯强度((428±87) MPa)提高了 43%, 断裂韧性((4.40±0.13) $MPa·m^{1/2}$)提高了 34%。此外, 与传统球磨混合工艺制备的试样相比, 强度和韧性也分别提高了 15%, 进一步证实该技术路线的有效性与先进性。

**关 键 词:** 石墨烯; 氧化铝; 复合陶瓷; 强韧化; 自组装

**中图分类号:** TQ174 **文献标志码:** A **文章编号:** 1000-324X(2026)04-0536-09

**Support Materials:**

# Fabrication of Graphene-reinforced Alumina Ceramic Composites *via* Adsorption-precipitation Self-assembly Combined with Spark Plasma Sintering

CHENG Aopeng[1,2,3], WANG Yuewen[2,3,4], XU Wentao[2,5,6], LIU Quanwei[2,3,4], ZHANG Haitao[2,5,6], ZHOU Youfu[2,5,6]

(1. College of Chemistry, Fuzhou University, Fuzhou 350108, China; 2. State Key Laboratory of Functional Crystals and Devices, Fujian Institute of Research on the Structure of Mater, Chinese Academy of Sciences, Fuzhou 350002, China; 3. Fujian College, University of Chinese Academy of Sciences, Fuzhou 350002, China; 4. College of Chemistry and Materials Science, Fujian Normal University, Fuzhou 350002, China; 5. Key Laboratory of Optoelectronic Materials Chemistry and Physics, Fujian Institute of Research on the Structure of Mater, Chinese Academy of Sciences, Fuzhou 350002, China; 6. Fujian Science & Technology Innovation Laboratory for Optoelectronic Information of China, Fuzhou 350108, China)

**Materials Information** $H_2SO_4$ (Sinopharm, AR); $H_3PO_4$ (Sinopharm, AR); flake graphite (Aladdin, 99.9%); $KMnO_4$ (Sinopharm, Industrial Grade); $H_2O_2$ (30% (in mass) in $H_2O$, Aladdin, AR); HCl (Sinopharm, AR)

**Synthesis of GO** First, 360 mL of $H_2SO_4$ and 40 mL of $H_3PO_4$ were poured into a 500 mL flask and placed in an ice-water bath. With continuous stirring, 3 g of flake graphite was slowly added to the solution, followed by incremental additions of 18 g of $KMnO_4$. Next, the flask was transferred to an oil bath at 50 ℃ and stirred for 5 h. When the temperature dropped to about 20 ℃, the product was slowly poured into 500 g of ice. Subsequently, 60 mL of $H_2O_2$ was added to react with the excess $KMnO_4$. The resulting slurry was centrifuged at 4000 r/min and washed several times with HCl and deionized water to remove the oxides remained. When pH of the solution was higher than 6, the precipitate (GO) was collected and freeze-dried for 48 h.

**Characterization of GO** As shown in Fig. S1(a), GO exhibits a pleated planar morphology with thicknesses in a nanometer scale and large lateral dimensions up to micrometer size. X-ray diffraction peak of GO is located at $2\theta$=10.5° with a wide width of half-height (Fig. S1(b)). The increased interlayer spacing of 0.842 nm (calculated by Bragg's formula) indicates the oxygen functional groups have been successfully intercalated into the carbon layer.

**TGA curve of precursor and GO** The precursor is thermally treated in an inert atmosphere to exhaust adsorbed water molecules, decompose the precipitated carbonates and hydroxides into alumina, as well as thermally reduce GO. As the TGA curve of precursor shown in Fig. S2, the weight loss is divided into three stages, in which a small amount of mass reduction below 100 ℃ is due to the evaporation of adsorbed moistures, followed by a rapid weight loss up to 250 ℃ attributed to the decomposition of the carbonate and GO functional groups, and then the mass decreases slowly, showing a plateau-like curve to 900 ℃ with a solid residue of 54%. For GO, the curves are similar, with a significant reduction in mass at 200 ℃ and a residual of about 37% after heat-treatment. Based on this result, the precursors were pre-calcined at 600 ℃ to avoid drastic weight changes and gas generation during the subsequent sintering of ceramic.

**Research on the densification of ceramic composites** The particle size, homogeneity and sintering activity of the composite powders are closely related to the microstructure and properties of the prepared ceramics. Taking 5rGO-$Al_2O_3$ system as a representative, the densification behavior at different temperatures was investigated to determine the optimal sintering parameters. As shown in Fig. S3(a-c), the displacement increases

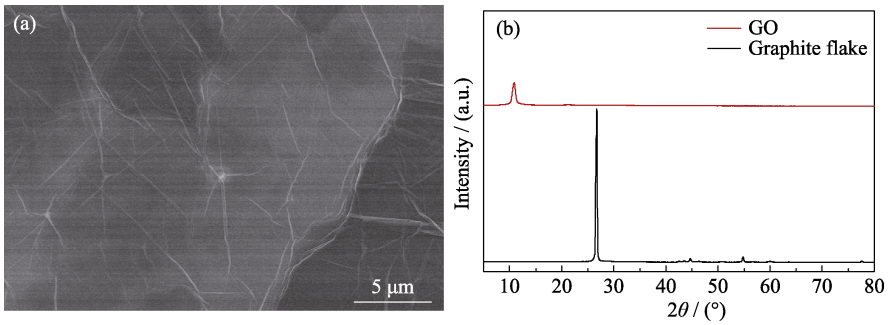


Fig. S1 (a) SEM image of obtained GO sheets; (b) XRD patterns of GO and original graphite powders

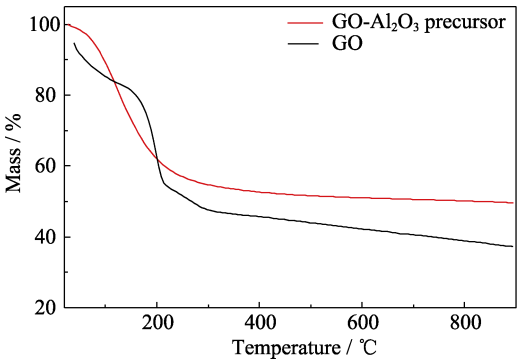


Fig. S2 TGA curves of GO and GO-$Al_2O_3$ precursor in $N_2$ atmosphere

slowly below 800 ℃, and then the densification rate rises sharply up to 1050 ℃ with significant shrinkage. After that the displacement maintains linear change, and the shrinkage of the dense sheet is basically completed during the isothermal stage. At the sintering temperature of 1300 ℃, continuous displacement during the isothermal holding stage reveals incomplete densification. In contrast, displacement stabilization observed at sintering temperatures of 1350 and 1400 ℃ confirms full densification completion. The bulk density of the samples gradually increases to 3.79 g·cm$^{-3}$ with enhancing sintering temperature from 1200 to 1350 ℃, while higher sintering temperature of 1400 ℃ does not promote further densification (Fig. S3(d)). Therefore, 1350 ℃ is set as the holding temperature for other specimens with different rGO contents, which is consistent with the reported densification temperature for wet chemical preparation of $Al_2O_3$ powders.

**Raman spectroscopy** For GO, the D and G peaks are observed to be located at 1356 and 1586 cm$^{-1}$, respectively. All the ceramic composites show similar spectral features, with the G peak near 1350 cm$^{-1}$, the D peak near 1590 cm$^{-1}$, and the 2D peak near 2700 cm$^{-1}$. The D and G peaks of the sintered samples are narrower and more distinctly separated than those of the powders, suggesting that the $sp^2$ carbon structure in the graphene planes is restored. In addition, the D band is shifted to 1350 cm$^{-1}$, indicating that rGO is subjected to tensile strain due to residual stresses between sheet and matrix. The ratio of the D peak intensity to the G peak intensity ($I_D/I_G$) is closely correlated with the degree of disorder and defects in graphene. The $I_D/I_G$ value of GO is 0.951, while much higher in ceramic composites, which is attributed to the interactions between graphene and $Al_2O_3$ along with structural defects induced by the sintering process.

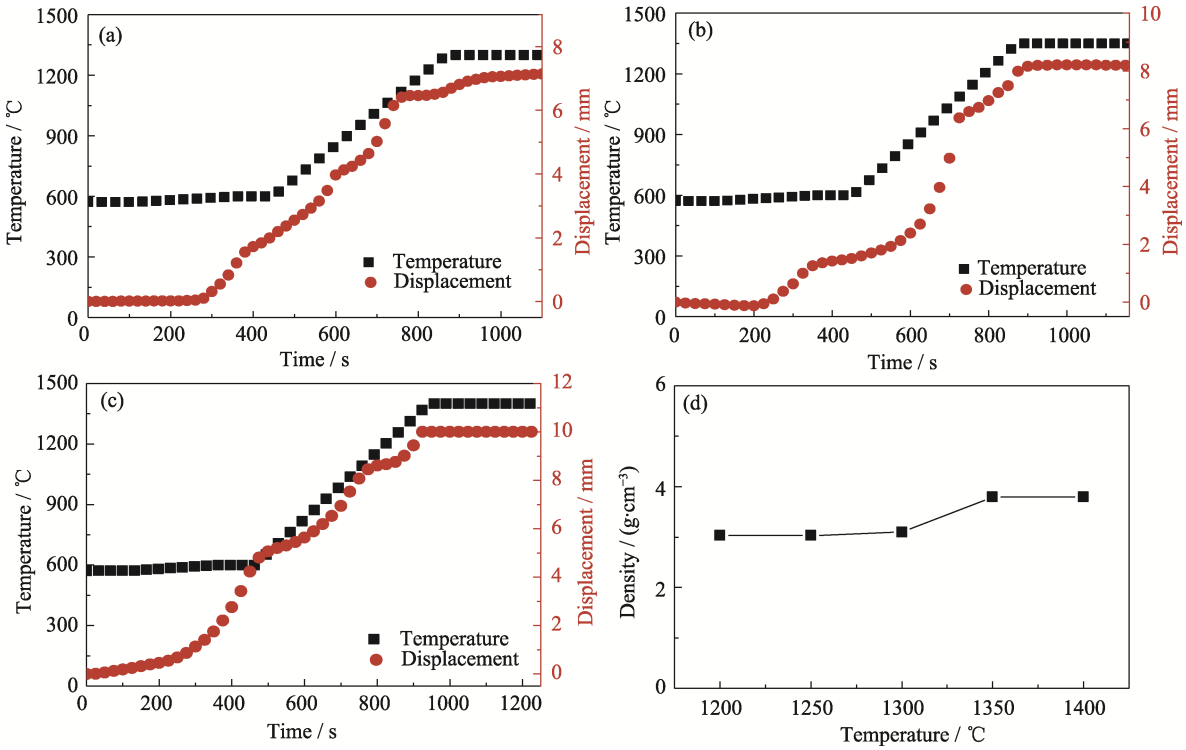


Fig. S3 (a-c) Sintering curves of 5rGO-$Al_2O_3$ composite ceramics and (d) bulk density of specimen sintered at different temperatures

(a) 1300 ℃; (b) 1350 ℃; (c) 1400 ℃

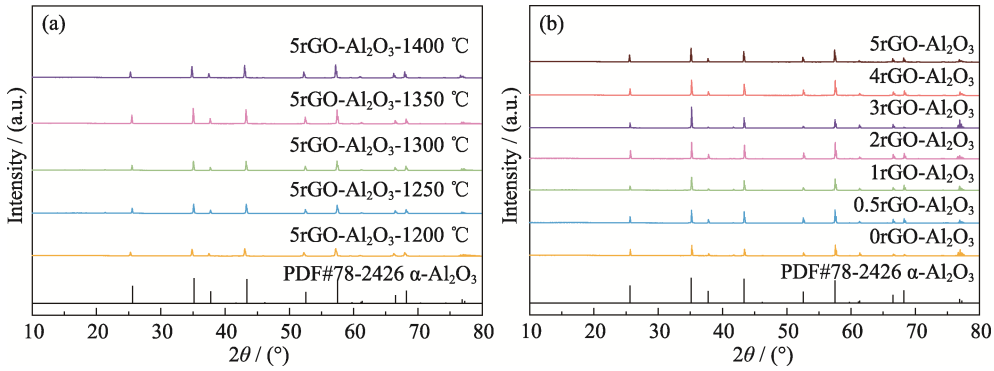


Fig. S4　(a) XRD patterns of 5rGO-$Al_2O_3$ ceramics at different temperatures and (b) rGO-$Al_2O_3$ ceramics with different rGO contents sintered at 1350 ℃

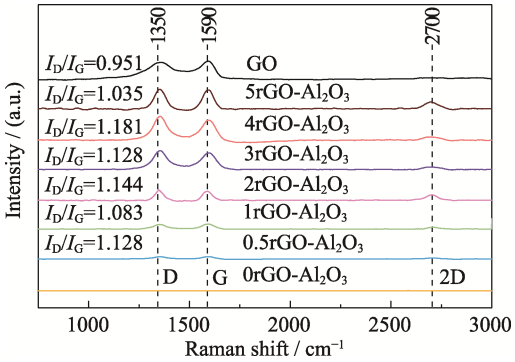


Fig. S5　Raman spectra of rGO-$Al_2O_3$ ceramic composites

## EDS mapping of ceramic

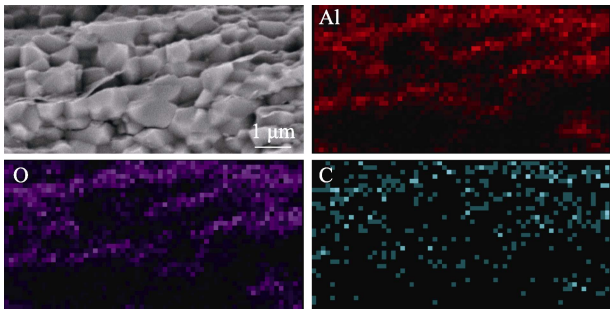


Fig. S6　EDS mappings of rGO-$Al_2O_3$ ceramic composites

## Thermal conductivity

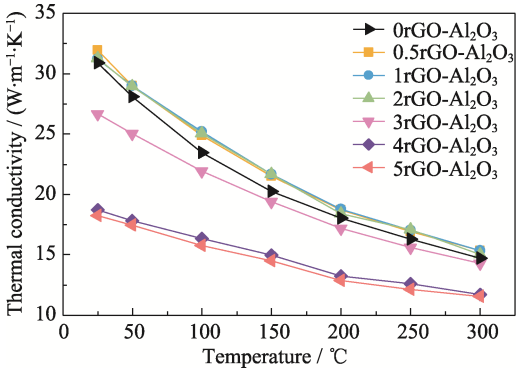


Fig. S7　Thermal conductivities of rGO-$Al_2O_3$ ceramic composites